



## RESEARCH ARTICLE

10.1029/2019GC008227

### Key Points:

- A genetic algorithm scheme statistically assesses the likelihood that the upper mantle contains melt from magnetotelluric data
- Melt distribution is heterogeneous, with the most likelihood for melt beneath hot spots and the least beneath cratons and old oceans
- Uncertainties in experimental constraints lead to substantially different results

### Correspondence to:

K. Selway,  
kate.selway@mq.edu.au

### Citation:

Selway, K., O'Donnell, J. P., & Özaydin, S. (2019). Upper mantle melt distribution from petrologically constrained magnetotellurics. *Geochemistry, Geophysics, Geosystems*, 20, 3328–3346. <https://doi.org/10.1029/2019GC008227>

Received 29 JAN 2019

Accepted 1 JUN 2019

Accepted article online 13 JUN 2019

Published online 12 JUL 2019

## Upper Mantle Melt Distribution From Petrologically Constrained Magnetotellurics

K. Selway<sup>1,2</sup> , J. P. O'Donnell<sup>3</sup> , and Sinan Özaydin<sup>1</sup>

<sup>1</sup>Department of Earth and Planetary Sciences, Macquarie University, Sydney, Australia, <sup>2</sup>Centre for Earth Evolution and Dynamics, University of Oslo, Oslo, Norway, <sup>3</sup>School of Earth and Environment, University of Leeds, Leeds, UK

**Abstract** Three parameters: temperature, hydrogen content, and the presence of partial melt, are the dominant controls on the rheology of the convecting upper mantle. As such, they determine the dynamics that control plate tectonics and continental evolution. Since hydrogen depresses the peridotite solidus temperature, these parameters are strongly linked petrologically. We have developed a genetic algorithm code to statistically assess the likelihood that a section of upper mantle contains partial melt. This code uses magnetotelluric observations and petrological constraints on composition and solidus temperatures and allows for uncertainties in the geotherm and the electrical conductivity structure. We have applied this code to the convecting upper mantle beneath (1) a stable continent (the Superior Craton); (2) a hot spot (Tristan da Cunha); (3) stable, old oceanic lithosphere (the northwest Pacific Ocean); and (4) young oceanic lithosphere (adjacent to the East Pacific Rise). Results show that the volume of melt in the convecting upper mantle is heterogeneous. The highest melt proportions are beneath the hot spot while little to no melt is required in the other regions. All regions show low water contents (generally <50 wt ppm in olivine) in the shallow convecting upper mantle, making it unlikely that water causes a large or sharp viscosity contrast between the lithosphere and the convecting mantle. Results differ significantly for different experimental olivine hydrogen conductivity models, highlighting the importance of reconciling these experimental constraints.

**Plain Language Summary** Plate tectonics occurs because the strong tectonic plates sit on underlying weaker and softer mantle that flows over geological timescales. We do not fully understand why this deeper mantle is weak—the two main contenders are that a small part of it is molten or that it contains nominal amounts of the element hydrogen. The electrical conductivity of the mantle is increased both by the presence of molten rock and by hydrogen, so when we interpret conductivity data, it is difficult to distinguish between these two interpretations. We have written a new code to help this. It analyzes whether the conductivity of the mantle could only be explained by the presence of molten rock, whether it could only be explained by large hydrogen contents, or whether it could be explained by either. Our results show that the distribution of partially molten rock is very uneven: Most lies beneath hot spot volcanic islands, while there is no need for molten rock to be present beneath old continents or old parts of the ocean. Beneath young parts of the ocean, the electrical conductivities could be explained by either a small amount of molten rock or by large hydrogen contents.

## 1. Introduction

Plate tectonics involves the movement of strong, lithospheric plates over weaker, convecting asthenosphere. Since the plate tectonics revolution in Earth sciences almost 50 years ago, the cause for this rheology contrast has been the subject of considerable debate (Chantel et al., 2016; Hirschmann, 2010; Karato, 2012, 2014; Stixrude & Lithgow-Bertelloni, 2005). Most processes that respond directly to upper mantle viscosity, such as glacial isostatic adjustment (e.g., Steffen & Kaufmann, 2005) and postseismic deformation (Hu et al., 2016; Masuti et al., 2016), suggest that there is a sharp decrease in viscosity between the lithosphere and asthenosphere. Temperature is a dominant control on upper mantle viscosity, but temperature changes smoothly and gradually between the lithosphere and asthenosphere, so it cannot be the cause of sharp viscosity changes. The two main candidates proposed to cause the sharp change in viscosity are (1) water residing in point defects in the main mineral constituents of the upper mantle, which are nominally anhydrous (Karato, 2012; Karato & Jung, 1998), and (2) a small amount of partial melt (Anderson & Spetzler, 1970; Hirschmann, 2010). Tiny amounts of either of these, of the order of tens to hundreds of parts per million

water and  $<<1\%$  partial melt, can decrease peridotite viscosity by more than an order of magnitude (Hirth & Kohlstedt, 2003; Holtzman, 2016) and cause a sharp change in viscosity between the lithosphere and asthenosphere. Asthenospheric peridotite water contents have been estimated from mid-ocean ridge (MOR) basalt compositions to be several hundreds of parts per million by weight, while lithospheric mantle xenoliths display a broad variation of water contents from essentially zero to asthenospheric values (Ingrin & Skogby, 2000; Peslier et al., 2010). The eruption of seamounts onto  $>70$ -Myr-old oceanic lithosphere suggests that it is feasible that partial melt exists throughout the oceanic asthenosphere. In this submission, we focus on using magnetotelluric (MT) data to better constrain the water and melt content of the asthenosphere in the hope that it will inform rheological models of the broader lithosphere-asthenosphere system.

These three factors that control rheology—temperature, peridotite water content, and the presence of partial melt—are not independent at upper mantle conditions since the solidus temperature of peridotite is strongly dependent on its water content (Hirschmann et al., 2009). Therefore, at a given temperature, an increasing water content will induce partial melting. Once melting occurs, water partitions preferentially into melt. This effectively limits the impact that water alone can have on mantle rheology: Extremely high peridotite water contents are not petrologically feasible, as they would induce melting, which would in turn reduce the peridotite water contents.

Temperature, water content, and the presence of partial melt are also the dominant controls on the electrical conductivity of the upper mantle as measured by MT data (e.g., Naif, 2018; Selway, 2014). The diffusion of hydrogen in nominally anhydrous mantle minerals (olivine, pyroxene, and garnet) carries charge and dramatically enhances the electrical conductivity of the minerals. Experimental studies agree that water contents as small as a few tens of parts per million by weight have a significant and measurable impact on electrical conductivity, although results from different laboratories disagree on the magnitude of this impact (e.g., Gardés et al., 2014; Poe et al., 2010; Wang et al., 2006; Yoshino et al., 2006). Melt is significantly more conductive than crystalline mantle rocks of typical compositions (Pommier & Le-Trong, 2011; Sifré et al., 2014), so the presence of any interconnected melt fraction will also produce a large jump in mantle conductivity. The conductivities of all major mantle materials also increase with increasing temperature.

The water content of the convecting upper mantle has been interpreted from MT data in numerous studies. Most of these interpretations focus on marine settings, where long MT deployments and a relatively homogeneous lithosphere mean that the asthenosphere is generally well resolved. A broad estimate of average asthenosphere conductivity was used by Wang et al. (2006) to infer an asthenosphere olivine water content of  $\sim 80$  wt ppm. At the subducting Cocos Plate, Naif et al. (2013) showed that partial melt must be present, arguing that if water alone were causing the observed conductivities, the water contents would have to be so high they would induce melting anyway. Sarafian et al. (2015) analyzed data from the stable central Pacific Ocean and showed that asthenosphere conductivities could be explained by a small amount of melt ( $<1\%$ ) but argued that they were more likely explained by melt-free peridotite containing between 25 and 400 wt ppm water. The only other large MT survey over old oceanic lithosphere was carried out in the northwest Pacific Ocean (Baba et al., 2013; Baba et al., 2017b). Utada and Baba (2014) showed that the asthenosphere conductivities could be explained by  $<0.5\%$  melt in peridotite but, similar to the central Pacific, the conductivities could also be explained by melt-free, hydrous peridotite. Two recent studies have helped to define the expected conductivity of upper mantle of typical composition. Naif (2018) estimated the maximum conductivity of melt-free upper mantle by forward modeling the conductivity of peridotite with a water content just below that which would induce melting. Katsura et al. (2017) forward modeled the conductivities of asthenosphere set to assumed depleted mantle and enriched mantle compositions. Their formulations included petrologically determined melting conditions and melt compositions. In both of these cases, the authors compared their forward models with inverse models of MT data from different oceanic regions, with some regions being matched by the forward models and others being distinct.

These examples of previous studies show that unambiguous interpretations of water contents and partial melt contents from MT data are often difficult to produce. In part, this is because certain conductivity ranges can be explained by either hydrated peridotite or partial melt (Figure 1). Some of this ambiguity can be resolved by considering petrological factors such as hydrogen-dependent solidus temperatures and the water contents of peridotite and melt in equilibrium (e.g., Katsura et al., 2017). However, this ambiguity is also due to inherent uncertainties. Uncertainties in asthenospheric geotherms easily reach  $50$ - $100$  °C (e.g., Katsura

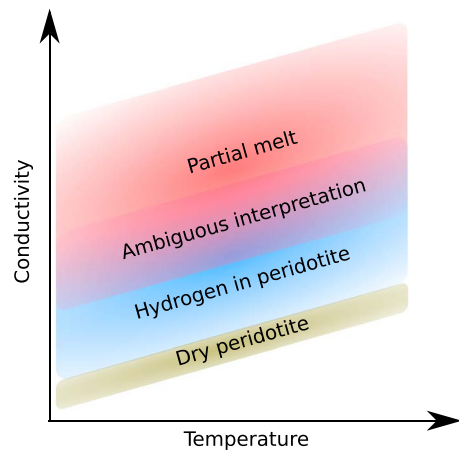


**Figure 1.** Schematic of the relationship between composition, temperature, and electrical conductivity at a standard oceanic adiabatic upper mantle geotherm. Dry (hydrogen-free) peridotite will produce the lowest conductivities. The highest conductivities can only be caused by the presence of partial melt. Intermediate between these are the conductivities caused by hydrated peridotite. There is an ambiguous range of conductivities that could be caused either by high water contents or by small amounts of partial melt. We seek to define this ambiguity by using a probabilistic approach to interpretation and to reduce it by using petrological constraints on the relationship between peridotite water content and melting.

et al., 2010) and uncertainties in electrical conductivities from inverted MT data easily reach half an order of magnitude. Different combinations of geotherm and conductivity for a given region can therefore often lead to different interpretations regarding peridotite hydrogen content and the presence or absence of partial melt. These disparate interpretations can be compounded by the use of different experimental constraints.

We present a new approach that inverts conductivity models directly for water content and the presence of partial melt while satisfying petrological constraints. We do this by means of a genetic algorithm (GA) code such that uncertainties in conductivity and temperature can be included in the inversion. The result of the inversion is a statistical analysis of the likelihood that partial melt is present as well as the ranges of temperatures, water contents, and melt contents that could produce the observed conductivity profile. This approach differs from those of Naif (2018) and Katsura et al. (2017) since it is an inverse scheme that inverts conductivity for temperature and composition, rather than a forward modeling scheme in which a temperature and composition are chosen and then compared with conductivity models. Although this is computationally more complex, it allows us to explore the full range of possible mantle compositions and geotherms without predefined assumptions. Several inversion schemes for interpreting thermochemical compositions from MT data have been presented in the past. Some of these use the LitMod framework (Afonso et al., 2008) and include multiple geophysical parameters (e.g., Fullea et al., 2011; Vozar et al., 2014) while others are stand-alone

schemes for conductivity data (e.g., Khan, 2016; Khan & Shankland, 2012). Our approach advances upon these earlier inverse schemes by including melt conductivity and a petrologically constrained melting process, while earlier schemes considered only solid-state minerals.

The inversion scheme uses a GA approach to statistically quantify the combinations of geotherms, upper mantle water contents, and partial melt contents that explain MT observations while satisfying petrological constraints. Starting from an initial population of geotherms and water contents, the algorithm drives evolution toward generations that better describe the MT observations, subject to the geotherms remaining within set uncertainty bounds and water contents remaining within solubility limits. Melting occurs if the peridotite is above its solidus temperature but ceases once the peridotite water content has reduced enough for it to be stable, with the water contents of the peridotite and melt remaining in equilibrium. Analysis of the fittest population allows statistical quantification of the various combinations of geotherms, water contents, and melt contents that can feasibly fit the data. If 100% of members of the fittest population infer the presence of melt, the data most likely require melt to be present. However, if a smaller proportion of members contain melt, it shows that the observed conductivity/temperature ranges could be explained by either partial melt or by high hydrogen contents. This formulation allows us to easily test the impact of different experimental formulations for mineral conductivity, hydrogen partition coefficients, and melt and rock geometry.

Previous results from inversion schemes for interpreting thermochemical compositions from MT data (e.g., Fullea et al., 2011; Khan, 2016; Khan & Shankland, 2012; Vozar et al., 2014) have shown that different formulations for mineral conductivities can have significant effects on final interpretations, as can petrophysical constraints such as hydrogen partition coefficients between minerals (e.g., Khan, 2016). While inversion results will necessarily be affected by many uncertain experimental parameters, we tested the impact of these parameters to clarify which experimental uncertainties have the most impact of MT interpretations.

## 2. Input Model Parameters

We applied the algorithm to MT data that image the convecting upper mantle in four regions with contrasting tectonic settings (Figure 2).

The first region is the Archean-Paleoproterozoic Superior Craton in central Minnesota, northern USA (Schmitz et al., 2006). This region was chosen to represent stable continental lithosphere. Few MT surveys

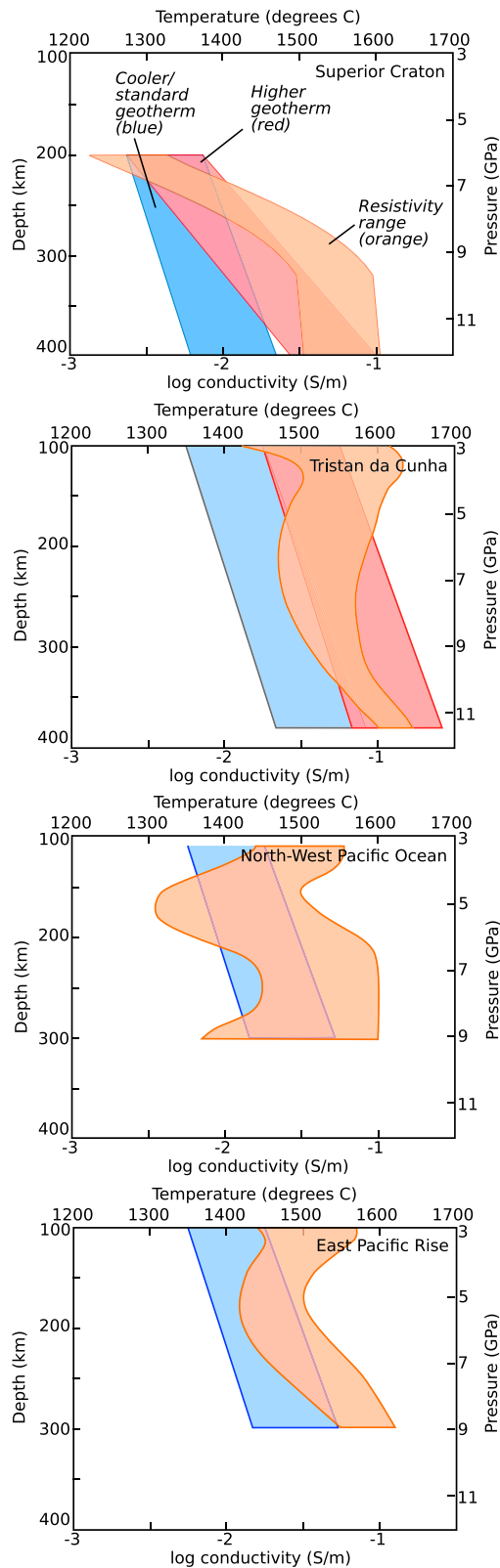


**Figure 2.** Magnetotelluric data (orange shading) from the Superior Craton, Tristan da Cunha hot spot, old oceanic lithosphere in the northwest Pacific Ocean, and young oceanic lithosphere adjacent to the East Pacific Rise, with low (blue) and high (red) geotherm ranges that were used in modeling.

are sufficiently extensive to constrain the conductivity of the asthenospheric mantle beneath stable continental lithosphere, but recent results from the USArray program now allow this region to be investigated. The MT data are taken from a profile at approximately 46.1°N, -95°E from the three-dimensional model of Yang et al. (2015) covering central USA. Lithospheric thickness in the region is estimated from seismic tomography models to be 200 km (Yuan et al., 2014). The temperature at 200-km depth has been estimated between 1,300 and 1,350 °C (Artemieva, 2006; Scully et al., 2004), so we set the temperature with 50 °C uncertainty to  $1,325 \pm 50$  °C. A standard asthenospheric adiabat of  $\sim 0.45$  °C/km (Katsura et al., 2010) produces a temperature of  $1,419.05 \pm 50$  °C at the 410-km discontinuity, which is much lower than the temperature of  $1,557 \pm 48$  °C estimated by Katsura et al. (2010) from petrological and experimental constraints. Therefore, we ran tests with two geotherms, one with a standard adiabat that was allowed to range between 0.42 and 0.48 °C/km (mantle potential temperatures [ $T_p$ ] of 1,179–1,291 °C) and the other with a much steeper adiabat ranging between 1.07 and 1.13 °C/km (producing even cooler  $T_p$  of 1,099–1,161 °C). Electrical resistivities from 200- to 400-km depth were extracted from the MT model of Yang et al. (2015). This model does not include information on tested resistivity ranges. Although they are not yet commonplace, Bayesian inversions of MT data are growing in popularity and will undoubtedly improve the meaningfulness of MT interpretations. Existing Bayesian methods (e.g., Conway et al., 2018) often produce uncertainties of approximately half an order of magnitude in resistivity, so this uncertainty was added to the data.

The second region is the Tristan da Cunha hot spot in the South Atlantic Ocean (Baba et al., 2017a). This region was chosen to represent young oceanic lithosphere with active volcanism. The Tristan da Cunha islands are an active hot spot, and geochemical data suggest they are fed by a plume that originates near the core-mantle boundary (Hoernle et al., 2015; Rohde et al., 2013). MT data were collected in a 550 km  $\times$  350 km grid covering seafloor ages spanning 10 to 30 Myr old. Baba et al., (2017a) ran a 3-D model of the MT data but did not image any structures resembling a plume extending into the mantle. Electrical resistivity ranges from 100- to 380-km depth were taken from the range of resistivities produced by 3D inversions of the region in Baba et al., (2017a). Again, models were run with two alternative geotherms. The first assumes a standard geotherm beneath 20-Myr-old oceanic lithosphere of  $1,400 \pm 50$  °C at 100-km depth (Grose & Afonso, 2013), increasing at a standard adiabat of 0.42 to 0.48 °C/km ( $T_p$  of 1,302–1,408 °C) since Geissler et al. (2017) used seismic data to infer typical, or even cold, temperatures at the mantle transition zone northwest of Tristan da Cunha. In contrast, Bonadio et al. (2018) used seismic shear wave velocities to infer a high mantle potential temperature beneath the Tristan da Cunha region, so the second model used a geotherm 100 °C hotter (with an uncertainty of  $\pm 50$  °C) than the first ( $T_p$  of 1,402–1,508 °C).

The third region is from oceanic lithosphere in the northwest Pacific Ocean (Baba et al., 2017b), which is among the oldest on Earth. This region was chosen to represent old, stable oceanic lithosphere that should be far removed from any melting associated with MOR volcanism. Electrical resistivity profiles between 110- and 300-km depth were taken from the 1-D model of the 130 Myr old “Area A” presented in

Baba et al. (2017b), with ranges taken from the published 95% uncertainty limits. Models were run with the temperature at 110-km depth taken from a standard plate cooling model (Grose & Afonso, 2013) to be  $1,405 \pm 50$  °C and the adiabat set to 0.42 and 0.48 °C/km ( $T_P$  of 1,302–1,408 °C).

The fourth region is from the Mantle Electromagnetic and Tomography (MELT) profile in the region of the East Pacific Rise (Baba et al., 2006; Evans et al., 2005). The MT data were collected in a region ~100 to 350 km east of the ridge crest, corresponding to seafloor ages of ~1.3 to 4.5 Myr. This is therefore outside of the region where voluminous melting is expected to occur, which was imaged by Key et al. (2013) to extend ~50 km either side of the East Pacific Rise. However, the data cover the region where small degree melts may still be present (e.g., Keller et al., 2017). Electrical resistivity was found to be anisotropic, and we took the upper and lower bounds of resistivity between 100- and 300-km depth from these anisotropic limits, as presented in Sarafian et al. (2015). The temperature at 100-km depth was taken from the standard plate cooling model to be  $1,400 \pm 50$  °C, and the adiabat was allowed to range between 0.42 and 0.48 °C/km ( $T_P$  of 1,302–1,408 °C).

### 3. Methods

#### 3.1. Mantle Composition

The GA scheme calculates conductivities of a standard upper mantle peridotite composition consisting of olivine, garnet, and pyroxene, with water stably partitioned between these phases. Pressure-dependent ( $P$ , in GPa) modal proportions of olivine ( $X_{Ol}$ ), garnet ( $X_{Gt}$ ), pyroxene ( $X_{Px}$ ), and the pyroxene aluminium content ( $C_{Al_2O_3}^{Px}$ ) were calculated as (Hirschmann et al., 2009):

$$X_{Ol} = 0.6 \quad (1)$$

$$X_{Gt} = 0.000297(P-3.2)^3 - 0.003128(P-3.2)^2 + 0.01545(P-3.2) + 0.135 \quad (2)$$

$$X_{Px} = 0.4 - X_{Gt} \quad (3)$$

$$C_{Al_2O_3}^{Px} = 6.88e^{-.4207(P-2.8)} + 0.05666P \quad (4)$$

Although these minerals are nominally anhydrous, they may contain small amounts of water, up to levels defined by their maximum water solubility. Where present, water will be distributed between the minerals in ratios defined by their partition coefficients. Since water is such a strong control on conductivity, it is important to include water solubilities and partition coefficients in conductivity calculations. Since the maximum solubility has been most closely studied in olivine, the GA scheme uses this value ( $C_{H_2O}^{Ol(max)}$ ) to define the overall peridotite maximum water solubility. Different experimental results constrain  $C_{H_2O}^{Ol(max)}$  differently. For most calculations, we used  $C_{H_2O}^{Ol(max)}$  of Ardia et al. (2012), which was calculated from the data of Ardia et al. (2012) and Tenner et al. (2012) at 1,450 °C and 5 to 13.4 GPa:

$$C_{H_2O}^{Ol(max)} = 39.1P - 66 \quad (5a)$$

We also tested the impact of using a different  $C_{H_2O}^{Ol(max)}$  from Withers and Hirschmann (2008), which was calculated from fitting a line to their olivine and pyroxene-bearing experimental data at 8 GPa and 1,000–1,600 °C ( $R^2 = -0.91$ ). This produces higher solubility limits than Ardia et al. (2012):

$$C_{H_2O}^{Ol(max)} = -2.1T + 3,728.6 \quad (5b)$$

After setting the olivine water content at a level between zero and  $C_{H_2O}^{Ol(max)}$ , the scheme then calculates the water contents of pyroxene and garnet using their partition coefficients ( $D$ ) with olivine. Again, there is considerable experimental uncertainty in these partition coefficients (Ardia et al., 2012; Khan, 2016). For most calculations we have used an aluminium-dependent partition coefficient between pyroxene and olivine ( $D_H^{Px/Ol}$ ) calculated by Ardia et al. (2012) from compiled experimental data:



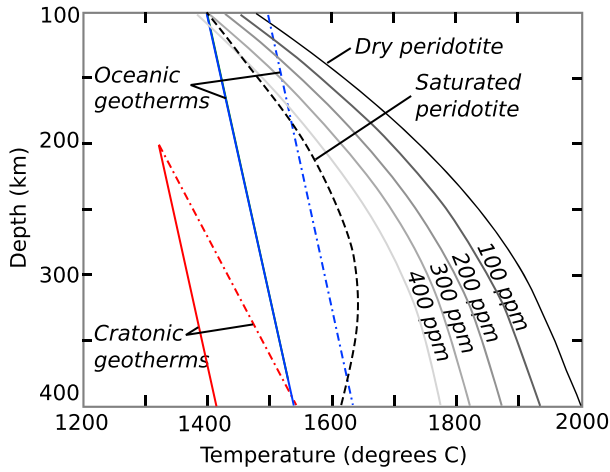


**Figure 3.** Dry, hydrous, and water-saturated peridotite solidus curves calculated from Hirschmann (2000) and Hirschmann et al. (2009) with saturation defined by Ardia et al. (2012). Blue lines show the oceanic geotherms used in the calculations (blue dashed line is the hotter Tristan da Cunha geotherm), and red lines show the continental geotherms used in the calculations (red dashed lined is the hotter Superior Craton geotherm). For clarity, the uncertainty ranges added to the geotherms in the calculations are not shown.

$$D_H^{Px/Ol} = 2.63 * C_{Al_2O_3}^{Px} + 0.78 \quad (6a)$$

To test the impact of  $D_H^{Px/Ol}$  on conductivity calculations, we also ran calculations using

$$D_H^{Px/Ol} = 1.3 \quad (6b)$$

from Tenner et al. (2012), calculated from experimental data collected at 10–13 GPa, which is at the deeper extent of our investigations. These authors state that this value is likely to be a minimum and to be higher in the shallow mantle, but it agrees well with the results of Ferot and Bolfan-Casanova (2012) at pressures >2.5 GPa.

There is considerable uncertainty in the partition coefficient between garnet and olivine, and values of  $D_H^{Gt/Ol}$  have been reported between <0.5 and 9 (Ardia et al., 2012; Mookherjee & Karato, 2010; Novella et al., 2014). For most calculations a value of 4.2 was used, but values of 0.5 and 9 were also tested:

$$D_H^{Gt/Ol} = 0.5, 4.2 \text{ or } 9 \quad (7)$$

The modal proportions and partition coefficients combine to give the peridotite water content:

$$C_{H_2O}^{Per} = C_{H_2O}^{Ol} \left( X_{Ol} + D_H^{Px} X_{Px} + D_H^{Gt} X_{Gt} \right) \quad (8)$$

### 3.2. Solidus Temperature

A key advantage of this code over previous schemes is its inclusion of petrologically constrained melting. To achieve this, the GA scheme uses the peridotite water content (defined above) to calculate the water-dependent peridotite solidus temperature. If the hydrated peridotite is above its solidus temperature, it melts; otherwise it is considered stable.

The solidus temperature (Figure 3) of dry peridotite (in degrees Celsius) up to 10 GPa is defined by (Hirschmann, 2000):

$$ST_{dry} = -5.14P^2 + 132.899P + 1,120.661 \quad (9)$$

At pressures greater than 10 GPa, the solidus temperature is given by (Hirschmann et al., 2009):

$$ST_{dry} = -1.092(P-10)^2 + 32.39(P-10) + 1,935 \quad (10)$$

The damp peridotite solidus ( $ST_{damp}$ , in degrees Celsius), where  $M$  is the molar mass of the melt and  $X_{OH}^{Melt}$  is the molar mass of hydroxyl ions in the melt, is taken from (Hirschmann et al., 2009):

$$ST_{damp} = \frac{ST_{dry}}{\left(1 - \frac{R}{0.4M}\right)} \log(1 - X_{OH}^{Melt}) \quad (11)$$

Hydrogen partitions strongly from peridotite into melt. The  $D_H^{Per/melt}$  partition coefficient is used both in the solidus temperature calculation (above; see Hirschmann et al., 2009, for more detail) and for determining the water contents of peridotite and melt during and after a melting event. Most models were run with partition coefficients of water between the peridotite minerals and an incipient melt from Hirschmann et al. (2009), but tests were also run using alternative partition coefficients from Tenner et al. (2012):

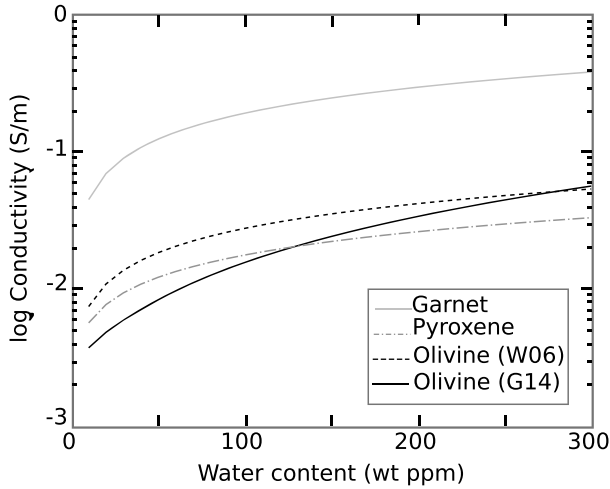


**Figure 4.** Water-content-dependent electrical conductivities of garnet (Dai & Karato, 2009b), pyroxene (Dai & Karato, 2009a), olivine using the Wang et al. (2006, W06) formulation, and olivine using the Gardés et al. (2014; G14) formulation calculated at a temperature of 1,500 K and a depth of 200 km.

$$D_H^{Ol/melt} = 0.0017 \quad (12)$$

(Hirschmann et al., 2009),or

$$D_H^{Ol/melt} = 0.0085 \quad (13)$$

(Tenner et al., 2012),

$$D_H^{Px/melt} = 0.0015 * C_{Al_2O_3}^{Px} + 0.0082 \quad (14)$$

(Hirschmann et al., 2009),or

$$D_H^{Px/melt} = 0.00515 \quad (15)$$

(Tenner et al., 2012),

$$D_H^{Gt/melt} = 0.003 \quad (16)$$

(Hirschmann et al., 2009), giving the partition coefficient of water between peridotite and an incipient melt,

$$D_H^{Per/melt} = (X_{Ol} * D_H^{Ol/melt}) + (X_{Px} * D_H^{Px/melt}) + (X_{Gt} * D_H^{Gt/melt}) \quad (17)$$

### 3.3. Electrical Conductivity

Through the previous calculations, the GA scheme calculates the composition of the asthenosphere, including the presence of melt and the water contents of the solid minerals and the melt. To invert MT data, these compositions must be converted into electrical conductivities. All experimental results show that water strongly affects olivine electrical conductivity, although the magnitude of this measured effect differs in results from different groups (e.g., Gardés et al., 2014; Poe et al., 2010; Wang et al., 2006; Yoshino et al., 2006; Figure 4). The strongest impact of water on olivine conductivity is suggested from the results of Wang et al. (2006) while the weakest impact of water on conductivity is suggested from the results of Yoshino et al. (2006). Gardés et al. (2014) considered the uncertainties in conductivity, temperature, and hydrogen content in different experimental results and produced a “unified” formulation that fit most of the experimental data.

To test the impact of different olivine hydrogen conduction models on geophysical interpretations, we ran all models using the formulations of both Wang et al. (2006) and Gardés et al. (2014). Wang et al. (2006) was chosen because it is able to match an observed conductivity with the lowest amount of hydrogen and will therefore be the least likely to melt—if melt is produced from Wang et al. (2006), it will certainly be produced from all other formulations. Gardés et al. (2014) was chosen because it is the only formulation that has sought to take into account errors and uncertainties and unify other experimental results. Our analysis does not seek to test the full range of experimental results, which would be well beyond the scope of this paper, but instead begins to explore the impacts these uncertainties can have on geophysical interpretations.

For an olivine hydrogen content of  $C_{H_2O}^{Ol}$  in weight percent, Wang et al. (2006) olivine conductivity due to hydrogen is

$$\sigma_{OlHyd}^{Wang} = (\sigma_{0\ hyd} * C_{H_2O}^{Ol} * e^{-\Delta H_{Hyd}/RT}) \quad (18)$$

while Gardés et al. (2014) olivine conductivity due to hydrogen ( $C_H^{Ol}$  in weight ppm) is

$$\sigma_{OlHyd}^{Gardes} = \sigma_{0\ hyd} * C_{H_2O}^{Ol} * e^{-(-\Delta H_{Hyd} - \alpha C_H^{Ol} * 0.333)/RT} \quad (19)$$

**Table 1**  
Parameters Used in Equations (18) to (22)

	Olivine (Gardes)	Olivine (Wang)	Pyroxene	Garnet
$\log \sigma_0_{pol}$ ( $\sigma$ in S/m)	2.34	2.34	—	—
$\Delta H_{pol}$ (J/mol)	144,000	144,000	—	—
$\log \sigma_0_{ion}$ ( $\sigma$ in S/m)	5.07	5.07	—	—
$\Delta H_{ion}$ (J/mol)	239,000	239,000	—	—
$\log \sigma_0_{hyd}$ ( $\sigma$ in S/m/wt ppm)	-1.37	3	2.6	3.29
$\Delta H_{hyd}$ (J/mol)	89,000	87,000	82,000	70,000 – ( $P * 5.7e^{-7}$ )
$\alpha$ (kJ/mol/wt ppm <sup>1/3</sup> )	2,080	—	—	—
$\log \sigma_{dry}$ ( $\sigma$ in S/m)	—	—	2.4	3.0154
$\Delta H_{dry}$ (J/mol)	—	—	147,000	128,000
$r$ exponent	—	0.62	0.62	0.63

Total olivine conductivity was calculated from conductivity due to polaron hopping ( $\sigma_{Olpol}$ ) and ionic conduction ( $\sigma_{Olion}$ ), both of which were taken from Gardés et al. (2014), and the hydrogen conduction defined above ( $\sigma_{OlHyd}^{Wang}$  or  $\sigma_{OlHyd}^{Gardes}$ ):

$$\sigma_{Ol} = \left( \sigma_0_{pol} e^{-\Delta H_{pol}/RT} \right) + \left( \sigma_0_{ion} e^{-\Delta H_{ion}/RT} \right) + \sigma_{OlHyd} \quad (20)$$

where  $R$  is the gas constant and  $T$  is the temperature in K.

Less extensive experimental work has been carried out on garnet and pyroxene conductivity. Garnet conductivity was taken as (Dai & Karato, 2009b)

$$\sigma_{gt} = \left( \sigma_0_{dry} e^{-\Delta H_{dry}/RT} \right) + \left( \sigma_0_{hyd} C_{H_2O}^{Gt} e^{-\Delta H_{Hyd}/RT} \right) \quad (21)$$

and pyroxene conductivity was taken as (Dai & Karato, 2009a)

$$\sigma_{pyx} = \left( \sigma_0_{dry} e^{-\Delta H_{dry}/RT} \right) + \left( \sigma_0_{hyd} * C_{H_2O}^{Pyx} e^{-\Delta H_{Hyd}/RT} \right) \quad (22)$$

The conductivity of melt varies depending on its temperature and composition (Pommier & Le-Trong, 2011), but at the melt proportions expected in the asthenosphere (<1%) the changes due to composition will have little effect on the bulk conductivity. The GA formulation calculates the water content of any melt, as it is set to be in equilibrium with the coexisting peridotite. Therefore, we chose to calculate melt conductivity using the water-dependent basaltic melt conductivity formulation of Sifré et al. (2014):

$$\sigma_{melt} = \sigma_0^{Melt} e^{E_{H_2O}/RT} \quad (23)$$

where

$$E_{H_2O} = 88774 e^{-3.88 * C_{H_2O}^{Melt}} + 73,029 \quad (24)$$

Mineral conductivities are plotted in Figure 4, and values for all parameters are given in Table 1. All calibrations have been normalized to the Bell calibration. Several experimental studies have shown that olivine conductivity increases when the olivine has undergone high strain (Caricchi et al., 2011; Pommier et al., 2015; Pommier et al., 2018; Zhang et al., 2014), as might be expected in the asthenosphere. However, these studies also suggest that this enhanced conductivity is a grain-size effect caused by dislocations activated during shearing and that this therefore is only likely to be an important factor controlling conductivities at grain sizes <<1 mm when grain boundary conduction begins to dominate (Pommier et al., 2018). Grain sizes in the asthenosphere are likely to be on the order of several tens to hundreds of millimeters (e.g., Behn et al., 2009), so we do not expect shearing to be a significant factor determining conductivity. Likewise, several studies have shown that the conductivity of rocks containing partial melt is anisotropic in the direction of strain (Caricchi et al., 2011; Pommier et al., 2015; Zhang et al., 2014), and anisotropic conductive zones near the lithosphere-asthenosphere boundary have been interpreted to be due to aligned



partial melt (Baba et al., 2006; Naif et al., 2013). However, at the temperatures and pressures deeper within the asthenosphere melt distribution is more likely to be isotropic (Pommier et al., 2015), so we have not directly included conductivity anisotropy. Any anisotropy present within the MT profiles will be accounted for in the resistivity bounds that have been applied.

These parameters allow the calculation of compositionally dependent conductivities of the solid peridotite and the melt. Since a continuous current can only pass through an interconnected conductive phase, the geometry of the peridotite minerals and the melt is important for determining the overall conductivity. The total resistivity was calculated from the resistivities of the solid matrix and the melt through a modified Archie's law (Glover, 2010), where for  $n$  phases with modal proportions  $\varphi$  the total conductivity  $\sigma$  is given by

$$\sigma = \sum_i^n \sigma_i \varphi_i^{m_i} \quad (25)$$

The modified Archie's law allows the geometric connection of the different components to be defined by the user. It contrasts with Hashin-Shtrikman bounds (Hashin & Shtrikman, 1963) used in most previous thermochemical inversion schemes (Fullea et al., 2011; Khan & Shankland, 2012) in which some connectivity is assumed and conductivity is dependent largely on the volume fractions of the different components. This contrast is important for phases like garnet, which tend to occur as isolated grains and are not expected to form an interconnected network at typical mantle compositions. The modified Archie's formulation contains an exponent ( $m$ ) for each phase that defines its interconnectivity, where  $m = 1$  for a perfectly connected phase and  $m$  increases with decreasing connectivity. The use of an Archie's law formulation allows us to test the impact of the connectivity of the melt phase, which is poorly known at upper mantle conditions (Laumonier et al., 2017). For the solid phase,  $m_{\text{Olivine}} = 1$ ,  $m_{\text{Pyroxene}} = 1.3$ , and  $m_{\text{Garnet}} = 5$ , reflecting the expected interconnectedness of the different phases.

### 3.4. Evolutionary Modeling

The equations described in the previous sections allow us to predict the expected composition, including melt, of a section of asthenosphere at a given temperature and hydrogen content and to calculate its expected electrical conductivity. To use these constraints to invert MT models for temperature and composition, we have used the GA optimization engine NSGA-II (Deb et al., 2002). This approach allows the interrelationships between temperature, water content, melting, and electrical conductivity to be taken into account. It also allows uncertainties in the geotherm and electrical conductivity structure to be included in the inversion. The results statistically quantify the combinations of geotherms, olivine water contents, and partial melt contents that can fit the MT profiles while satisfying experimental constraints. This approach allows us to clearly distinguish the different regions in Figure 1 since the analysis identifies the subsurface conductivities that can only be caused by either melt-free peridotite or by peridotite with partial melt present, and those that could be caused by either.

The code was designed to converge on the geotherms and hydrogen contents that best explain the conductivity data in a petrologically plausible manner. As in the mantle, if the peridotite in the model is at a temperature exceeding its hydrogen-dependent solidus temperature (equation (17)), melting occurs. During melting, hydrogen partitions preferentially into the melt (equation (13)), thereby dehydrating the peridotite and increasing its solidus temperature. The algorithm sets melting to proceed iteratively in increments of 0.0001 wt%. As melting proceeds, the peridotite dehydrates. Melting ceases once the peridotite dehydrates sufficiently that the solidus temperature meets or exceeds the geotherm.

The geotherm and hydrogen profiles were parameterized as second-order polynomial and cubic Bezier curves, respectively, and the coefficients of these curves are the parameters that the algorithm seeks to optimize. For the temperature profile, the first coefficient is the temperature at the shallowest modeled depth, the second coefficient defines the adiabatic gradient, and the third coefficient controls the degree of permitted curvature in the profile (i.e., deviation from adiabaticity). Four equidistant control points define the cubic Bezier hydrogen profile. At each control point the hydrogen content is constrained to be less than the maximum hydrogen solubility in peridotite at that depth.

Sixty pairs of geotherm and hydrogen profiles with coefficients satisfying the imposed constraints are randomly generated to serve as an initial population for the GA. If modeled hydrogen and temperature profiles can explain the conductivity data within uncertainty bounds, the associated coefficients are ranked fit, and

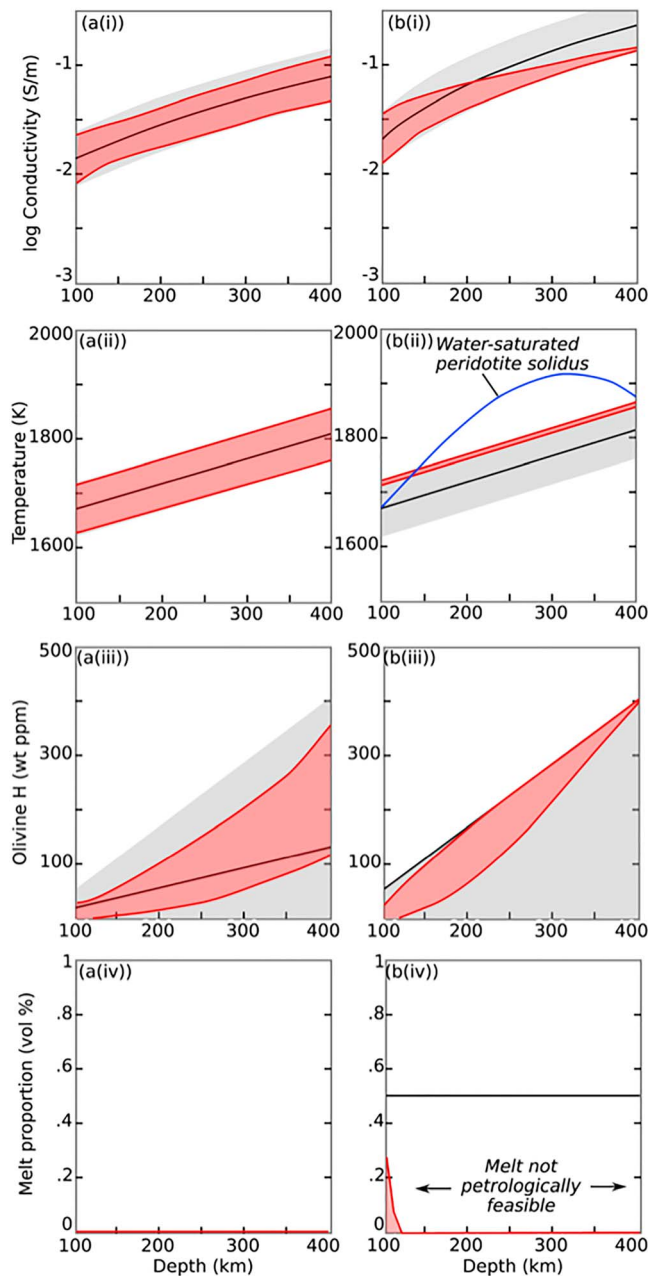


**Figure 5.** Results of genetic algorithm (GA) inversions run of forward models with known compositions and geotherms. Black lines show forward modeled conductivities, geotherms, and water contents, and gray shading shows the bounds and ranges for these parameters used in the inversions. Red shading shows the ranges of parameters produced by the best fitting GA populations. (a) Input model is melt free, and the peridotite water content is one third of saturation. (b) Input model is water saturated and contains 0.5% melt even though melt is only stable at shallow depths, shown by the intersection of the geotherm with the water-saturated peridotite solidus (blue line). The GA inversion does not produce melt at depths where it is not petrologically feasible.

their genetic information is propagated to the next generation. The genetic information of unfit population members is discarded. Evolution through 50 generations (using crossover and mutation probabilities of 0.9 and 0.05, respectively) was sufficient to arrive at the suite of temperature and hydrogen profiles best explaining the observed conductivities; evolution beyond this point yielded no discernible improvements in data fitting.

To test the utility of the scheme, inversions were run of several forward models with known compositions and geotherms (Figure 5). For melt-free peridotite with a water content one third of the maximum solubility defined by Ardia et al. (2012) at a standard oceanic asthenosphere geotherm, the forward-modeled conductivity is given by the black line in Figure 5a(i). Uncertainties on the conductivity and temperature profiles and bounds on the water contents for the GA scheme are shown by the gray-shaded regions. The red-shaded regions show the ranges of conductivities, geotherms, and water contents produced by the best fitting populations produced by the GA scheme. All input constraints are satisfied, and no melt is modeled. A second model is presented to demonstrate the importance of the petrological constraints in the GA scheme. A petrologically unfeasible forward model was produced that is water saturated and also contains 0.5% melt throughout the model region even though temperatures only exceed the solidus temperature in the uppermost asthenosphere. Since it is not petrologically permissible for melt to be present at greater depths, the GA scheme only models melt from 100- to 120-km depth. At greater depths, the GA scheme models conductivities at the lowest extent of the input range and models temperatures and water contents at the highest extents of their bounds as it seeks to produce the high input conductivities without the presence of melt.

#### 4. Results

All regions were modeled using both the Gardés et al. (2014) and Wang et al. (2006) formulations for hydrous olivine conductivity, hereafter referred to as G14 and W06, respectively. Figure 6 displays the results for models run with cooler geotherms, an Archie's melt connection exponent of 1.5, a maximum hydrogen solubility defined by equation (5) (Ardia et al., 2012), an aluminium-dependent  $D_H^{Px/Ol}$  (equation (6); Ardia et al., 2012), and an olivine/garnet hydrogen partition coefficient of 4.2. Figure 7 displays the results of models run to test conditions of hotter geotherms, lower melt connection exponents, and alternative water solubilities and partition coefficients.

Superior Craton models were run with two different geotherms—one with a standard adiabat (Figure 6a) and one with a steeper adiabat to match predicted temperatures at the 410-km discontinuity (Figure 7a). No melting was produced in any of the models. The impact of water on olivine conductivity is stronger in the W06 conductivity formulation than the G14 conductivity formulation, and this is reflected in the results, which show lower water contents for the W06 models than the G14 models for both geotherms. Water contents are also impacted by the geotherm, with higher average water contents required to match the observed conductivity at cooler geotherms than hotter geotherms.

Models of the asthenosphere beneath the Tristan da Cunha islands were also run with two different geotherms—one derived from a standard

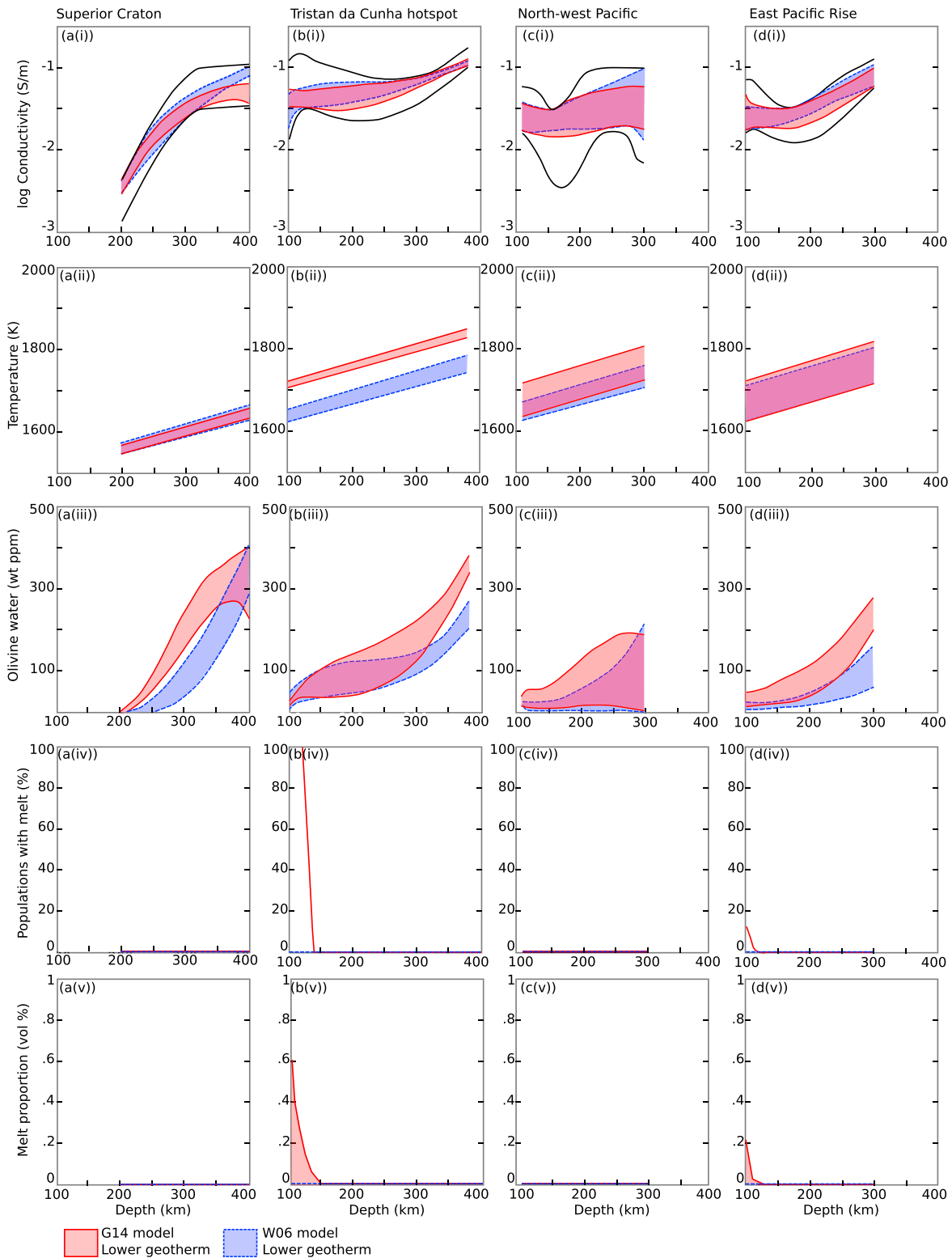


**Figure 6.** Results of the genetic algorithm analysis for models run at cooler geotherms, an Archie’s melt connection exponent of 1.5, a maximum hydrogen solubility defined by equation (5) (Ardia et al., 2012), an aluminium-dependent  $D_H^{px/Ol}$  (equation (6); Ardia et al., 2012), and an olivine/garnet hydrogen partition coefficient of 4.2, using both the Gardés et al. (2014; G14) and the Wang et al. (2006; W06) olivine conductivity models. Results show electrical conductivity (i), where the black lines are the input MT conductivity ranges, temperature (ii), olivine hydrogen content (iii), the percentage of final populations that contain any partial melt (iv), and the proportion of that melt (v) for data from the Superior Craton (a), Tristan da Cunha hot spot (b), old oceanic lithosphere in the north-west Pacific (c), and young oceanic lithosphere near the East Pacific Rise (d).

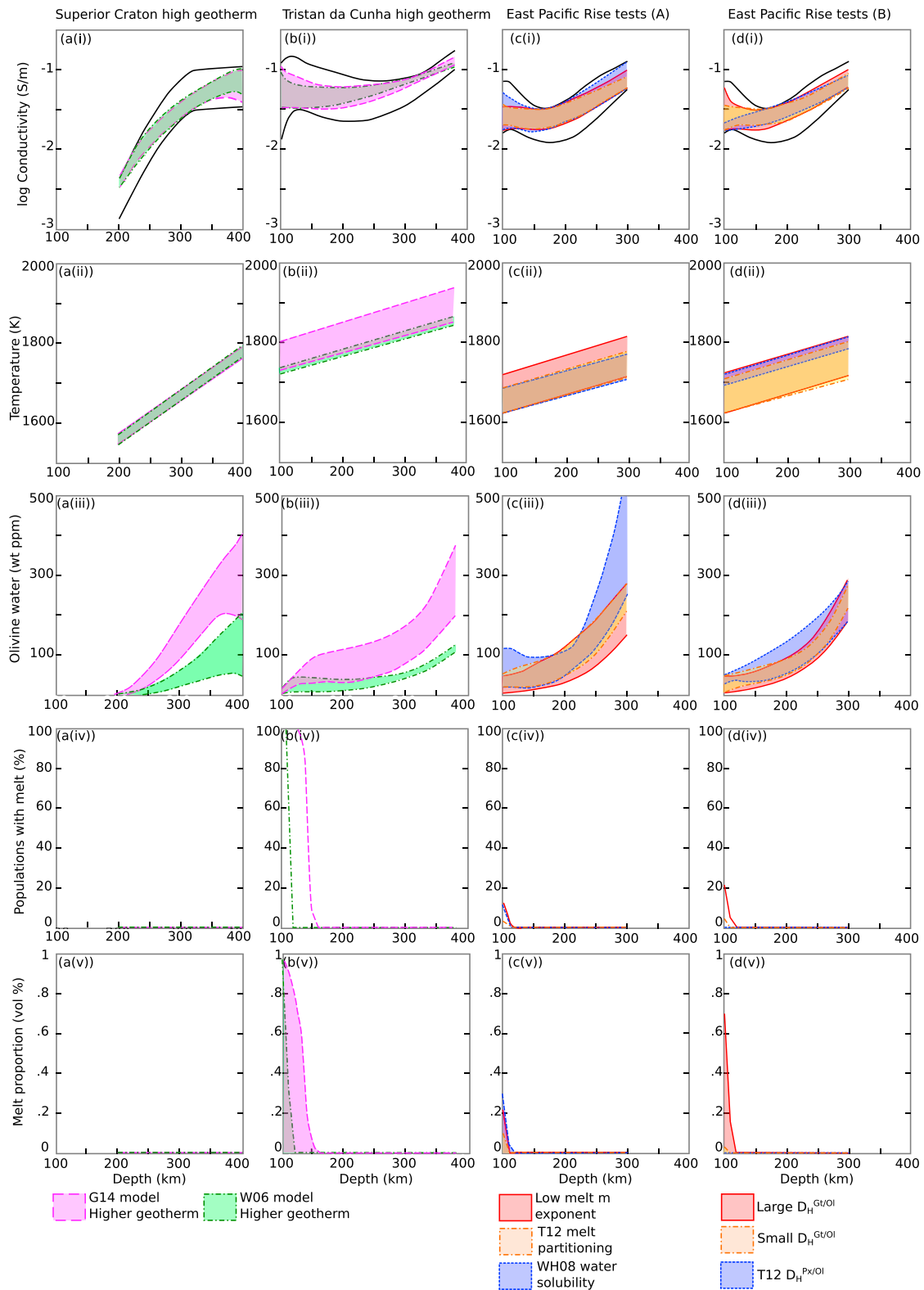


**Figure 7.** Results of the genetic algorithm analysis for models run to test the impact of alternative model parameters, namely, hotter geotherms for the Superior Craton (a) and Tristan da Cunha (b) data sets. Panels (c) and (d) show tests run on the East Pacific Rise data set to test the impact of alternative experimental parameters, namely, (a) improved melt connectivity (Archie's law exponent  $m = 1.3$ ), solid/melt water partitioning defined by Tenner et al. (2012) and maximum peridotite water solubility defined by Withers and Hirschmann (2008) and (b) alternative  $D_H^{Gt/Ol}$  values of 0.5 and 9, and  $D_H^{Px/Ol}$  defined by Tenner et al. (2012). All model tests were run with only the Gardés et al. (2014; G14) olivine conductivity model.

plate cooling model (Figure 6b) and the other increased by 100 °C to reflect a possible enhanced mantle potential temperature (Figure 7b). All models except the cooler W06 model require some melt to be present. In the cooler geotherm G14 model (Figure 6b), up to 100% of final populations contain up to 0.6% melt from 100- to 140-km depth. At the hotter geotherm (Figure 7b) the pattern is similar, with up to 100% of final populations containing up to 1% melt from 100- to 150-km depth. The hotter geotherm W06 model (Figure 7b) has up to 100% of final populations containing up to 0.97% melt from 100- to 110-km depth. Olivine water contents increase with depth are lower for the W06 models than the G14 models and are depressed in all model regions where there is significant melting.

Models of the asthenosphere beneath the northwest Pacific Ocean were only run with a standard adiabat since the geotherm in this region is relatively well constrained. Neither the W06 nor the G14 model produced any melt. Olivine water contents of the final populations are also modest, to a maximum of ~50 wt ppm in the shallow asthenosphere and a maximum of ~200 wt ppm in the deeper asthenosphere. Average olivine water contents from the W06 models are lower than those from the G14 models, and water contents of both models increase with depth. While the inverted conductivities in the northwest Pacific Ocean fit the input constraints, the inverted models do not replicate the strong variations in conductivity with depth seen in the MT model. This feature is also apparent to a lesser extent in the models from the other regions. This is due to the smoothness constraints put on the geotherms and the water contents. While the current smoothness constraints can fit the input conductivities, larger variations in water content with depth would be necessary to produce larger variations in conductivity with depth.

Models of the region adjacent to the East Pacific Rise were run at only one geotherm (Figure 6d). Little melting was modeled: The W06 model did not produce any melt, and the G14 model produced up to 0.22% melt from 100- to 110-km depth in 10% of the final populations. Olivine water contents are moderate, and the W06 hydrogen contents (<50 wt ppm at 100-km depth increasing to <200 wt ppm at 300-km depth) are lower than the G14 hydrogen contents (<50 wt ppm at 100-km depth increasing to <300 wt ppm at 300-km depth).

Additional model tests were run with the East Pacific Rise data set (Figures 6c and 6d). All tests were run using the G14 olivine formulation, and all other parameters were consistent with the models described above apart from the parameter being tested. The first test changed the Archie's formulation melt connection exponent from 1.5 to 1.3 to test the impact of an improved melt connection. Results (Figure 7c) showed no significant change in melt proportions modeled. The second test investigated the impact of different partition coefficients of water between the solid peridotite and the melt by using the partition coefficients of Tenner et al. (2012). This produced slightly less melting, with <5% of populations containing up to ~0.1% melt from 100- to 110-km depth. The third test was run with maximum water solubility in olivine derived from the data of Withers and Hirschmann (2008). These results suggested larger maximum water solubilities than those of Ardia et al. (2012), and this is reflected in higher olivine water contents (Figure 7c). However, this has not resulted in significant changes to the melting patterns.

The remaining tests investigated the impact of solid-state water partitioning between olivine, pyroxene, and garnet. Partitioning between garnet and hydrogen is poorly constrained (Ardia et al., 2012; Mookherjee & Karato, 2010; Novella et al., 2014), so tests were run at the upper and lower extremities of the experimental ranges ( $D_H^{Gt/Ol} = 0.5$  and 9). These changes do have a measurable impact on the amount of melting produced (Figure 7d). As  $D_H^{Gt/Ol}$  increases, an increasing proportion of populations contains melt (up to 22%), and the proportion of melt also increases (up to 0.7%). Finally, the impact of partitioning between pyroxene and olivine ( $D_H^{Px/Ol}$ ) was tested by using  $D_H^{Px/Ol} = 1.3$  from Tenner et al. (2012), which gives a smaller partition coefficient than that used in the other models. This also has a significant effect on the results, with no melt being produced (Figure 7d).

## 5. Discussion

### 5.1. Upper Mantle Melt Distribution

The GA formulation is conservative with regard to melting and treats the hypothesis that the asthenosphere contains hydrogen but no partial melt as the “null hypothesis.” Each generation starts from a melt-free, hydrous composition, and if this melt-free composition can match the observed conductivity, there is no impetus to melt. There are three potential melting outcomes in the model results: First, 100% of the



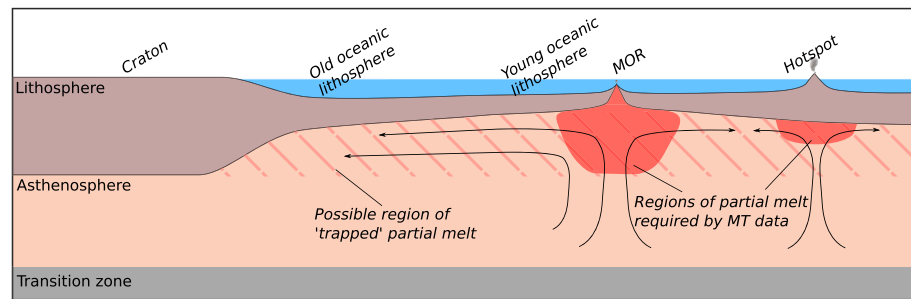


**Figure 8.** Cartoon of the possible distribution of partial melt in the convecting upper mantle. Results from this analysis of magnetotelluric (MT) data suggest that melt must exist in the shallow asthenosphere beneath the Tristan da Cunha hot spot and that it may extend several hundred kilometers from the East Pacific Rise mid-ocean ridge in the shallow asthenosphere. It is possible that a small amount of melt also exists throughout the shallow oceanic asthenosphere (hashed region), causing the sharp viscosity contrast between the lithosphere and the asthenosphere and the seismic low-velocity zone, but this is not required by the MT data.

populations may melt, indicating that the MT observations can only be explained by the presence of melt. Second, an intermediate percentage of final populations may contain melt. This shows that the interpretation is ambiguous and MT observations can be explained either by hydrous peridotite or by partial melt. Third, none of the final populations may contain melt. This shows that hydrous peridotite can account for the MT observations and there is no impetus for the model peridotite to melt. However, since the absence of melt is the null hypothesis, this result does not mean that there are no compositions containing partial melt that could hypothetically fit the MT data.

Results show that melt distribution in the shallow upper mantle is spatially heterogeneous (Figure 8). As is perhaps not unexpected, the strongest evidence for melt and the largest melt contents lie beneath the Tristan da Cunha hot spot, which is believed to be caused by a mantle plume potentially originating from the core-mantle boundary (Hoernle et al., 2015; Rohde et al., 2013). Here, in the shallow asthenosphere, most model parameter combinations require the presence of significant amounts of melt (up to 1%). The only other region where melt was modeled in the shallow asthenosphere is close to the East Pacific Rise, although the presence of melt here is more ambiguous, and the observed conductivities can also be explained by hydrous peridotite. In both the Superior Craton and northwest Pacific Ocean, the observed conductivities can be produced by hydrated peridotite without any need for partial melt.

## 5.2. Impact of Model Parameters

A consistent challenge in producing compositional interpretations of MT data is that different experimental laboratories produce different relationships between conductivity and composition, especially when considering the effect of water on olivine conductivity. It is beyond the scope of one paper to test all possible combinations of model parameters, but we tested the impact of different conductivity formulations by running all models with the olivine conductivity formulations of Gardés et al. (2014) and Wang et al. (2006). Results for every model region consistently show that olivine hydrogen contents are lower for the W06 formulation than the G14 formulation and that more melting is modeled when the G14 formulation is used. We chose the W06 formulation, as it is the most conservative and will produce the minimum possible distribution of melt. Other formulations that are not shown here, such as those of Yoshino et al. (2006), predict that the impact of hydrogen on conductivity is smaller than both W06 and G14 and would therefore produce higher water contents and more melt than these results. The results do show consistent patterns regarding melt distribution; for instance, melt is present beneath Tristan da Cunha and is absent beneath the Superior Craton and northwest Pacific Ocean regardless of the conductivity formulation used. However, the significant differences in hydrogen content modeled using G14 and W06, and the inconsistency between melting results in the East Pacific Rise highlight the importance of reconciling the experimental mineral physics data sets.

There is also considerable uncertainty in many other experimental mineral physics and petrology constraints used in this analysis. To explore which of these parameters are likely to have the biggest impact on MT interpretations in the asthenosphere, we tested different values for melt connection, maximum

water solubility, and partitioning of water between the peridotite and the melt as well as between the solid-state minerals within the peridotite. Results show that most of these parameters have measurable impacts on the GA results (Figures 7c and 7d) but that these impacts are smaller than those caused by the choice of conductivity model.

If a melt fraction is better connected (lower melt connectivity exponent [ $m$ ]), a given conductivity can be matched with a smaller melt proportion, so it is expected that this change reduces the modeled melt proportions, as observed (Figure 7d). The melt connectivity exponent has no bearing on whether hydrous peridotite can reach conductivities high enough to match the MT data, so a similar proportion of models should melt regardless of the value of  $m$ , as is also observed. Increasing the maximum water solubility in olivine (and, by extension, peridotite) produces models that, unsurprisingly, contain larger olivine water contents. Temperatures are concomitantly slightly lower to produce a match to the conductivities. However, there is little change in the melting patterns because the melting is also constrained by the solidus temperature and because the model will only invoke melting if a hydrous peridotite composition cannot match the conductivity constraints. The solid-state partition coefficients have notable effects on the results.  $D_H^{Gt/Ol}$  affects both the garnet and peridotite water contents. Higher garnet water contents from high  $D_H^{Gt/Ol}$  increase garnet conductivity, but this has little impact on total conductivity at the modeled garnet modal proportions. However, the resultant higher peridotite water content means that peridotite is more likely to melt with a higher  $D_H^{Gt/Ol}$ , as is observed (Figure 7d). Similarly, the lower  $D_H^{Px/Ol}$  values of Tenner et al. (2012) result in lower overall peridotite water contents and lower degrees of melting (Figure 7d).

While our results show that uncertainties in most model parameters do not produce differences as large as those from the different conductivity models, they do also show that improving these constraints would allow clearer interpretations of mantle composition to be developed from geophysical data. In particular, improved estimates of partition coefficients would significantly improve the reliability of MT interpretations. Differences in other model parameters not tested here, such as melt molar mass and damp peridotite solidus temperature definitions, are also likely to affect results in a way that is measurable but smaller than differences in the conductivity models. In the meantime, the results also show that it is important for interpreters to be aware of the impact that their choices of experimental parameters could have on their interpretation and to update inversion schemes as new experimental constraints become available.

### 5.3. Hydrogen Contents and the Cause of the Lithosphere/Asthenosphere Viscosity Contrast

Two features are consistent in all model results. The first is that average olivine water contents increase with depth in the asthenosphere. In general, models run with the W06 olivine formulation contain slightly lower proportions of olivine water than models run with the G14 formulation, but the difference between the formulations generally does not exceed a few tens of weight parts per million. In the uppermost ~50 km of the asthenosphere, average water contents in almost all models are <50 wt ppm. At greater depths within the asthenosphere, olivine water contents rise to generally between 100 and 400 wt ppm. The second feature is that melt is seldom required to interpret the MT data. Given the setup of the GA scheme, where melt is only present if the peridotite is above its solidus temperature, melt is only required to be present at shallow depths beneath the Tristan da Cunha plume, and it may be present in the shallow asthenosphere beneath young oceanic lithosphere near the East Pacific Rise.

It is difficult to argue that the low water contents modeled in the upper asthenosphere, which are similar to those measured from the continental lithosphere (Demouchy & Bolfan-Casanova, 2016), could be responsible for a sharp or large change in viscosity between the lithosphere and asthenosphere (e.g., Karato, 2014). This leaves partial melt as the most likely cause for this viscosity contrast. Partial melt is also the most likely explanation for the seismic low velocity zone in the upper asthenosphere (Nettles & Dziewoński, 2008), especially given that hydrogen does not seem to be a viable explanation since it does not affect seismic attenuation (Cline et al., 2018; Selway & O'Donnell, 2019), and our models show no peak in hydrogen content at low velocity zone depths (Figures 5 and 6). The difficulty with this interpretation is that the MT models do not require partial melt in the shallow asthenosphere either. This apparent contradiction could be explained by the model recently proposed by Selway and O'Donnell (2019). In this model, a small amount of melt is trapped in the asthenosphere after it melts at MORs or hot spots (Figure 8). It remains trapped in the host peridotite as the asthenosphere convects away from the MOR, causing the low-velocity zone. Since this

melt formed under high geotherm conditions and is trapped, it can be present even after the host peridotite cools below its solidus temperature. It will therefore not be modeled by this GA scheme, which only allows melt to be present if the peridotite is above its solidus temperature due to high hydrogen contents and temperatures. This “trapped melt” model also predicts the pattern of peridotite water contents that have been produced here. In the shallow asthenosphere, the peridotite has melted at MORs and will therefore be dehydrated. As the degree of MOR melting decreases with depth, peridotite water contents will increase.

## 6. Conclusions

Electrical conductivities in the convecting upper mantle (the asthenosphere) that are higher than those expected for dry peridotite can be caused either by hydrous peridotite or the presence of partial melt. Distinguishing between these interpretations can often be difficult because many conductivities could be attributed to either factor and also because of uncertainties in modeled conductivities, mantle geotherms, and various experimental mineral physics and petrology constraints. We have investigated the causes of asthenosphere conductivity in a quantitative statistical way using self-consistent petrological constraints. We use a GA optimization engine to explore temperature and peridotite water profiles capable of explaining observed conductivities. Evolution proceeds from an initial population of peridotite with water contents and temperatures within set bounds. If the peridotite at those conditions would melt, melting occurs in small increments until the peridotite is sufficiently dehydrated that melting stops. The electrical conductivity of the model (either with or without melt) is calculated, and, if it lies within the observed conductivity ranges, the model is ranked fit, and its genetic material propagates through to the next generation. Evolution proceeds to an optimized “fittest” generation. In this way, quantitative statistics regarding the distribution of peridotite geotherms, water contents, and melt contents that match the conductivity observations are developed.

Results show that asthenosphere melt distribution is heterogeneous. Of the four regions investigated (the Superior Craton, the Tristan da Cunha hot spot, the north-west Pacific Ocean, and adjacent to the East Pacific Rise), the strongest evidence for the presence of melt is in the shallow asthenosphere beneath the Tristan da Cunha hot spot, where most combinations of experimental parameters suggest partial melt must be present. Beneath the young oceanic lithosphere adjacent to the East Pacific Rise, results show that electrical conductivities in the shallow asthenosphere could be caused by either hydrated peridotite or by partial melt. The results do not suggest that partial melt is required in any of the other asthenospheric regions investigated.

Interpretations of geophysical data require experimental petrology and mineral physics data, many of which are not well constrained. The GA approach allows the impact of different experimental parameters to be easily tested. We have tested three parameters likely to have the biggest impacts on interpretations: the olivine water conductivity model (Gardés et al., 2014; Wang et al., 2006), the water partition coefficients between the solid-state minerals and between the solid peridotite and the melt, and the degree of melt connection. Results show that the different olivine conductivity models have a large impact on the interpretation, with the Wang et al. (2006) model consistently producing lower hydrogen contents and melt proportions than the Gardés et al. (2014) model. Uncertainties in partition coefficients also have a significant impact on the reliability of MT interpretations. Improved experimental constraints will lead to more robust geophysical interpretations.

## Acknowledgments

K. S. received support from Australian Research Council Grant FT150100541 and the Research Council of Norway through Centre of Excellence project 223272. J. P. O. D. was supported by the Natural Environment Research Council Grant NE/L006065/1. No new data are presented in this article; existing data can be sourced via their respective publications.

## References

- Afonso, J. C., Fernandez, M., Ranalli, G., Griffin, W., & Connolly, J. (2008). Integrated geophysical-petrological modeling of the lithosphere and sublithospheric upper mantle: Methodology and applications. *Geochemistry, Geophysics, Geosystems*, 9, Q05008. <https://doi.org/10.1029/2007GC001834>
- Anderson, D. L., & Spetzler, H. (1970). Partial melting and the low-velocity zone. *Physics of the Earth and Planetary Interiors*, 4(1), 62–64. [https://doi.org/10.1016/0031-9201\(70\)90030-0](https://doi.org/10.1016/0031-9201(70)90030-0)
- Ardia, P., Hirschmann, M., Withers, A., & Tenner, T. (2012). H<sub>2</sub>O storage capacity of olivine at 5–8 GPa and consequences for dehydration partial melting of the upper mantle. *Earth and Planetary Science Letters*, 345, 104–116.
- Artemieva, I. M. (2006). Global 1×1 thermal model TC1 for the continental lithosphere: Implications for lithosphere secular evolution. *Tectonophysics*, 416(1–4), 245–277. <https://doi.org/10.1016/j.tecto.2005.11.022>
- Baba, K., Chave, A. D., Evans, R. L., Hirth, G., & Mackie, R. L. (2006). Mantle dynamics beneath the East Pacific Rise at 17 S: Insights from the Mantle Electromagnetic and Tomography (MELT) experiment. *Journal of Geophysical Research*, 111, B02101. <https://doi.org/10.1029/2004JB003598>

- Baba, K., Chen, J., Sommer, M., Utada, H., Geissler, W. H., Jokat, W., & Jegen, M. (2017a). Marine magnetotellurics imaged no distinct plume beneath the Tristan da Cunha hotspot in the southern Atlantic Ocean. *Tectonophysics*, 716, 52–63. <https://doi.org/10.1016/j.tecto.2016.09.033>
- Baba, K., Tada, N., Matsuno, T., Liang, P., Li, R., Zhang, L., et al. (2017b). Electrical conductivity of old oceanic mantle in the northwestern Pacific I: 1-D profiles suggesting differences in thermal structure not predictable from a plate cooling model. *Earth, Planets and Space*, 69(1), 111. <https://doi.org/10.1186/s40623-017-0697-0>
- Baba, K., Tada, N., Zhang, L., Liang, P., Shimizu, H., & Utada, H. (2013). Is the electrical conductivity of the northwestern Pacific upper mantle normal? *Geochemistry, Geophysics, Geosystems*, 14, 4969–4979. <https://doi.org/10.1002/2013GC004997>
- Behn, M. D., Hirth, G., & Elsenbeck, J. R. II (2009). Implications of grain size evolution on the seismic structure of the oceanic upper mantle. *Earth and Planetary Science Letters*, 282(1–4), 178–189. <https://doi.org/10.1016/j.epsl.2009.03.014>
- Bonadio, R., Geissler, W. H., Lebedev, S., Fullea, J., Ravenna, M., Celli, N. L., et al. (2018). Hot upper mantle beneath the Tristan da Cunha Hotspot, from probabilistic Rayleigh-wave inversion and petrological modeling. *Geochemistry, Geophysics, Geosystems*, 19, 1412–1428. <https://doi.org/10.1002/2017GC007347>
- Caricchi, L., Gaillard, F., Mecklenburgh, J., & Le Trong, E. (2011). Experimental determination of electrical conductivity during deformation of melt-bearing olivine aggregates: Implications for electrical anisotropy in the oceanic low velocity zone. *Earth and Planetary Science Letters*, 302(1–2), 81–94. <https://doi.org/10.1016/j.epsl.2010.11.041>
- Chantel, J., Manthilake, G., Andrault, D., Novella, D., Yu, T., & Wang, Y. (2016). Experimental evidence supports mantle partial melting in the asthenosphere. *Science Advances*, 2(5). <https://doi.org/10.1126/sciadv.1600246>
- Cline, C., Faul, U., David, E., Berry, A., & Jackson, I. (2018). Redox-influenced seismic properties of upper-mantle olivine. *Nature*, 555(7696), 355–358. <https://doi.org/10.1038/nature25764>
- Conway, D., Simpson, J., Didana, Y., Rugari, J., & Heinson, G. (2018). Probabilistic magnetotelluric inversion with adaptive regularisation using the No-U-Turns sampler. *Pure and Applied Geophysics*, 175(8), 2881–2894. <https://doi.org/10.1007/s00024-018-1870-5>
- Dai, L., & Karato, S.-I. (2009a). Electrical conductivity of orthopyroxene: Implications for the water content of the asthenosphere. *Proceedings of the Japan Academy, Series B*, 85(10), 466–475.
- Dai, L., & Karato, S.-I. (2009b). Electrical conductivity of pyrope-rich garnet at high temperature and high pressure. *Physics of the Earth and Planetary Interiors*, 176(1–2), 83–88. <https://doi.org/10.1016/j.pepi.2009.04.002>
- Deb, K., Pratap, A., Agarwal, S., & Meyarivan, T. (2002). A fast and elitist multiobjective genetic algorithm: NSGA-II. *IEEE Transactions on Evolutionary Computation*, 6(2), 182–197. <https://doi.org/10.1109/4235.996017>
- Demouchy, S., & Bolfan-Casanova, N. (2016). Distribution and transport of hydrogen in the lithospheric mantle: A review. *Lithos*, 240, 402–425.
- Evans, R. L., Hirth, G., Baba, K., Forsyth, D., Chave, A., & Mackie, R. (2005). Geophysical evidence from the MELT area for compositional controls on oceanic plates. *Nature*, 437(7056), 249–252. <https://doi.org/10.1038/nature04014>
- Ferot, A., & Bolfan-Casanova, N. (2012). Water storage capacity in olivine and pyroxene to 14 GPa: Implications for the water content of the Earth's upper mantle and nature of seismic discontinuities. *Earth and Planetary Science Letters*, 349, 218–230.
- Fullea, J., Muller, M., & Jones, A. (2011). Electrical conductivity of continental lithospheric mantle from integrated geophysical and petrological modeling: Application to the Kaapvaal Craton and Rehoboth Terrane, southern Africa. *Journal of Geophysical Research*, 116, B10202. <https://doi.org/10.1029/2011JB008544>
- Gardés, E., Gaillard, F., & Tarits, P. (2014). Toward a unified hydrous olivine electrical conductivity law. *Geochemistry, Geophysics, Geosystems*, 15, 4984–5000. <https://doi.org/10.1002/2014GC005496>
- Geissler, W. H., Jokat, W., Jegen, M., & Baba, K. (2017). Thickness of the oceanic crust, the lithosphere, and the mantle transition zone in the vicinity of the Tristan da Cunha hot spot estimated from ocean-bottom and ocean-island seismometer receiver functions. *Tectonophysics*, 716, 33–51. <https://doi.org/10.1016/j.tecto.2016.12.013>
- Glover, P. W. (2010). A generalized Archie's law for n phases. *Geophysics*, 75(6), E247–E265. <https://doi.org/10.1190/1.3509781>
- Grose, C. J., & Afonso, J. C. (2013). Comprehensive plate models for the thermal evolution of oceanic lithosphere. *Geochemistry, Geophysics, Geosystems*, 14, 3751–3778. <https://doi.org/10.1002/ggge.20232>
- Hashin, Z., & Shtrikman, S. (1963). A variational approach to the theory of the elastic behaviour of multiphase materials. *Journal of the Mechanics and Physics of Solids*, 11(2), 127–140. [https://doi.org/10.1016/0022-5096\(63\)90060-7](https://doi.org/10.1016/0022-5096(63)90060-7)
- Hirschmann, M. M. (2000). Mantle solidus: Experimental constraints and the effects of peridotite composition. *Geochemistry, Geophysics, Geosystems*, 1(10). <https://doi.org/10.1029/2000GC000070>
- Hirschmann, M. M. (2010). Partial melt in the oceanic low velocity zone. *Physics of the Earth and Planetary Interiors*, 179(1–2), 60–71. <https://doi.org/10.1016/j.pepi.2009.12.003>
- Hirschmann, M. M., Tenner, T., Aubaud, C., & Withers, A. (2009). Dehydration melting of nominally anhydrous mantle: The primacy of partitioning. *Physics of the Earth and Planetary Interiors*, 176(1–2), 54–68. <https://doi.org/10.1016/j.pepi.2009.04.001>
- Hirth, G., & Kohlstedt, D. (2003). *Rheology of the upper mantle and the mantle wedge: A view from the experimentalists. Inside the subduction Factory*, (pp. 83–105).
- Hoernle, K., Rohde, J., Hauff, F., Garbe-Schönberg, D., Homrighausen, S., Werner, R., & Morgan, J. P. (2015). How and when plume zonation appeared during the 132 Myr evolution of the Tristan Hotspot. *Nature Communications*, 6(1), 7799. <https://doi.org/10.1038/ncomms8799>
- Holtzman, B. K. (2016). Questions on the existence, persistence, and mechanical effects of a very small melt fraction in the asthenosphere. *Geochemistry, Geophysics, Geosystems*, 17, 470–484. <https://doi.org/10.1002/2015GC006102>
- Hu, Y., Bürgmann, R., Banerjee, P., Feng, L., Hill, E. M., Ito, T., et al. (2016). Asthenosphere rheology inferred from observations of the 2012 Indian Ocean earthquake. *Nature*, 538(7625), 368–372. <https://doi.org/10.1038/nature19787>
- Ingrin, J., & Skogby, H. (2000). Hydrogen in nominally anhydrous upper-mantle minerals: Concentration levels and implications. *European Journal of Mineralogy*, 12(3), 543–570. <https://doi.org/10.1127/ejm/12/3/0543>
- Karato, S.-i. (2012). On the origin of the asthenosphere. *Earth and Planetary Science Letters*, 321, 95–103.
- Karato, S.-i. (2014). Does partial melting explain geophysical anomalies? *Physics of the Earth and Planetary Interiors*, 228, 300–306. <https://doi.org/10.1016/j.pepi.2013.08.006>
- Karato, S.-i., & Jung, H. (1998). Water, partial melting and the origin of the seismic low velocity and high attenuation zone in the upper mantle. *Earth and Planetary Science Letters*, 157(3–4), 193–207. [https://doi.org/10.1016/S0012-821X\(98\)00034-X](https://doi.org/10.1016/S0012-821X(98)00034-X)
- Katsura, T., Baba, K., Yoshino, T., & Kogiso, T. (2017). Electrical conductivity of the oceanic asthenosphere and its interpretation based on laboratory measurements. *Tectonophysics*, 717, 162–181. <https://doi.org/10.1016/j.tecto.2017.07.001>



- Katsura, T., Yoneda, A., Yamazaki, D., Yoshino, T., & Ito, E. (2010). Adiabatic temperature profile in the mantle. *Physics of the Earth and Planetary Interiors*, 183(1-2), 212–218. <https://doi.org/10.1016/j.pepi.2010.07.001>
- Keller, T., Katz, R. F., & Hirschmann, M. M. (2017). Volatiles beneath mid-ocean ridges: Deep melting, channelised transport, focusing, and metasomatism. *Earth and Planetary Science Letters*, 464, 55–68. <https://doi.org/10.1016/j.epsl.2017.02.006>
- Key, K., Constable, S., Liu, L., & Pommier, A. (2013). Electrical image of passive mantle upwelling beneath the northern East Pacific Rise. *Nature*, 495(7442), 499–502. <https://doi.org/10.1038/nature11932>
- Khan, A. (2016). On Earth's mantle constitution and structure from joint analysis of geophysical and laboratory-based data: An example. *Surveys in Geophysics*, 37(1), 149–189. <https://doi.org/10.1007/s10712-015-9353-z>
- Khan, A., & Shankland, T. (2012). A geophysical perspective on mantle water content and melting: Inverting electromagnetic sounding data using laboratory-based electrical conductivity profiles. *Earth and Planetary Science Letters*, 317, 27–43.
- Laumonier, M., Farla, R., Frost, D. J., Katsura, T., Marquardt, K., Bouvier, A.-S., & Baumgartner, L. P. (2017). Experimental determination of melt interconnectivity and electrical conductivity in the upper mantle. *Earth and Planetary Science Letters*, 463, 286–297. <https://doi.org/10.1016/j.epsl.2017.01.037>
- Masuti, S., Barbot, S. D., Karato, S.-i., Feng, L., & Banerjee, P. (2016). Upper-mantle water stratification inferred from observations of the 2012 Indian Ocean earthquake. *Nature*, 538(7625), 373–377. <https://doi.org/10.1038/nature19783>
- Mookherjee, M., & Karato, S. i. (2010). Solubility of water in pyrope-rich garnet at high pressures and temperature. *Geophysical Research Letters*, 37, L03310. <https://doi.org/10.1029/2009GL041289>
- Naif, S. (2018). An upper bound on the electrical conductivity of hydrated oceanic mantle at the onset of dehydration melting. *Earth and Planetary Science Letters*, 482, 357–366. <https://doi.org/10.1016/j.epsl.2017.11.024>
- Naif, S., Key, K., Constable, S., & Evans, R. (2013). Melt-rich channel observed at the lithosphere-asthenosphere boundary. *Nature*, 495(7441), 356–359. <https://doi.org/10.1038/nature11939>
- Nettel, M., & Dziewoński, A. M. (2008). Radially anisotropic shear velocity structure of the upper mantle globally and beneath North America. *Journal of Geophysical Research*, 113, B02303. <https://doi.org/10.1029/2006JB004819>
- Novella, D., Frost, D. J., Hauri, E. H., Bureau, H., Raepsaet, C., & Roberge, M. (2014). The distribution of H<sub>2</sub>O between silicate melt and nominally anhydrous peridotite and the onset of hydrous melting in the deep upper mantle. *Earth and Planetary Science Letters*, 400, 1–13. <https://doi.org/10.1016/j.epsl.2014.05.006>
- Peslier, A. H., Woodland, A. B., Bell, D. R., & Lazarov, M. (2010). Olivine water contents in the continental lithosphere and the longevity of cratons. *Nature*, 467(7311), 78–81. <https://doi.org/10.1038/nature09317>
- Poe, B. T., Romano, C., Nestola, F., & Smyth, J. R. (2010). Electrical conductivity anisotropy of dry and hydrous olivine at 8 GPa. *Physics of the Earth and Planetary Interiors*, 181(3-4), 103–111. <https://doi.org/10.1016/j.pepi.2010.05.003>
- Pommier, A., Kohlstedt, D. L., Hansen, L. N., Mackwell, S., Tasaka, M., Heidelbach, F., & Leinenweber, K. (2018). Transport properties of olivine grain boundaries from electrical conductivity experiments. *Contributions to Mineralogy and Petrology*, 173, 1–13.
- Pommier, A., Leinenweber, K., Kohlstedt, D. L., Qi, C., Garner, E. J., Mackwell, S. J., & Tyburczy, J. A. (2015). Experimental constraints on the electrical anisotropy of the lithosphere-asthenosphere system. *Nature*, 522(7555), 202–206. <https://doi.org/10.1038/nature14502>
- Pommier, A., & Le-Trong, E. (2011). "SIGMELTS": A web portal for electrical conductivity calculations in geosciences. *Computers & Geosciences*, 37(9), 1450–1459. <https://doi.org/10.1016/j.cageo.2011.01.002>
- Rohde, J., Hoernle, K., Hauff, F., Werner, R., O'Connor, J., Class, C., et al. (2013). 70 Ma chemical zonation of the Tristan-Gough hotspot track. *Geology*, 41(3), 335–338. <https://doi.org/10.1130/G33790.1>
- Sarafian, E., Evans, R. L., Collins, J. A., Elsenbeck, J., Gaetani, G. A., Gaherty, J. B., et al. (2015). The electrical structure of the central Pacific upper mantle constrained by the NoMelt experiment. *Geochemistry, Geophysics, Geosystems*, 16, 1115–1132. <https://doi.org/10.1002/2014GC005709>
- Schmitz, M., Bowring, S., Southwick, D., Boerboom, T., & Wirth, K. (2006). High-precision U-Pb geochronology in the Minnesota River Valley subprovince and its bearing on the Neoproterozoic to Paleoproterozoic evolution of the southern Superior Province. *Geological Society of America Bulletin*, 118(1-2), 82–93. <https://doi.org/10.1130/B25725.1>
- Scully, K. R., Canil, D., & Schulze, D. J. (2004). The lithospheric mantle of the Archean Superior Province as imaged by garnet xenocryst geochemistry. *Chemical Geology*, 207(3-4), 189–221. <https://doi.org/10.1016/j.chemgeo.2004.03.001>
- Selway, K. (2014). On the causes of electrical conductivity anomalies in tectonically stable lithosphere. *Surveys in Geophysics*, 35(1), 219–257. <https://doi.org/10.1007/s10712-013-9235-1>
- Selway, K., & O'Donnell, J. (2019). A small, unextractable melt fraction as the cause for the low velocity zone. *Earth and Planetary Science Letters*, 517, 117–124. <https://doi.org/10.1016/j.epsl.2019.04.012>
- Sifré, D., Gardés, E., Massuyeau, M., Hashim, L., Hier-Majumder, S., & Gaillard, F. (2014). Electrical conductivity during incipient melting in the oceanic low-velocity zone. *Nature*, 509(7498), 81–85. <https://doi.org/10.1038/nature13245>
- Steffen, H., & Kaufmann, G. (2005). Glacial isostatic adjustment of Scandinavia and northwestern Europe and the radial viscosity structure of the Earth's mantle. *Geophysical Journal International*, 163(2), 801–812. <https://doi.org/10.1111/j.1365-246X.2005.02740.x>
- Stixrude, L., & Lithgow-Bertelloni, C. (2005). Mineralogy and elasticity of the oceanic upper mantle: Origin of the low-velocity zone. *Journal of Geophysical Research*, 110, B03204. <https://doi.org/10.1029/2004JB002965>
- Tenner, T. J., Hirschmann, M. M., Withers, A. C., & Ardia, P. (2012). H<sub>2</sub>O storage capacity of olivine and low-Ca pyroxene from 10 to 13 GPa: Consequences for dehydration melting above the transition zone. *Contributions to Mineralogy and Petrology*, 163(2), 297–316. <https://doi.org/10.1007/s00410-011-0675-7>
- Utada, H., & Baba, K. (2014). Estimating the electrical conductivity of the melt phase of a partially molten asthenosphere from seafloor magnetotelluric sounding data. *Physics of the Earth and Planetary Interiors*, 227, 41–47. <https://doi.org/10.1016/j.pepi.2013.12.004>
- Vozar, J., Jones, A. G., Fullea, J., Agius, M. R., Lebedev, S., Le Pape, F., & Wei, W. (2014). Integrated geophysical-petrological modeling of lithosphere-asthenosphere boundary in central Tibet using electromagnetic and seismic data. *Geochemistry, Geophysics, Geosystems*, 15, 3965–3988. <https://doi.org/10.1002/2014GC005365>
- Wang, D., Mookherjee, M., Xu, Y., & Karato, S.-i. (2006). The effect of water on the electrical conductivity of olivine. *Nature*, 443(7114), 977–980. <https://doi.org/10.1038/nature05256>
- Withers, A. C., & Hirschmann, M. M. (2008). Influence of temperature, composition, silica activity and oxygen fugacity on the H<sub>2</sub>O storage capacity of olivine at 8 GPa. *Contributions to Mineralogy and Petrology*, 156(5), 595–605. <https://doi.org/10.1007/s00410-008-0303-3>
- Yang, B., Egbert, G. D., Kelbert, A., & Meqbel, N. M. (2015). Three-dimensional electrical resistivity of the north-central USA from EarthScope long period magnetotelluric data. *Earth and Planetary Science Letters*, 422, 87–93. <https://doi.org/10.1016/j.epsl.2015.04.006>
- Yoshino, T., Matsuzaki, T., Yamashita, S., & Katsura, T. (2006). Hydrous olivine unable to account for conductivity anomaly at the top of the asthenosphere. *Nature*, 443(7114), 973–976. <https://doi.org/10.1038/nature05223>



- Yuan, H., French, S., Cupillard, P., & Romanowicz, B. (2014). Lithospheric expression of geological units in central and eastern North America from full waveform tomography. *Earth and Planetary Science Letters*, *402*, 176–186. <https://doi.org/10.1016/j.epsl.2013.11.057>
- Zhang, B., Yoshino, T., Yamazaki, D., Manthilake, G., & Katsura, T. (2014). Electrical conductivity anisotropy in partially molten peridotite under shear deformation. *Earth and Planetary Science Letters*, *405*, 98–109. <https://doi.org/10.1016/j.epsl.2014.08.018>